MIT Open Access Articles

Mixing dynamics in bubbling fluidized beds

Massachusetts Institute of Technology

Mixing dynamics in bubbling fluidized beds

A. Bakshi[a,*], C. Altantzis[a,b], A.F. Ghoniem[a]

[a]Massachusetts Institute of Technology, Department of Mechanical Engineering
77 Massachusetts Ave., Cambridge, MA 02139, USA
[b]National Energy Technology Laboratory, Morgantown, WV 26507, USA

Abstract

Solids mixing affects thermal and concentration gradients in fluidized bed reactors and is, therefore, critical to their performance. Despite substantial effort over the past decades, understanding of solids mixing continues to be lacking because of technical limitations of diagnostics in large pilot and commercial-scale reactors. This study is focused on investigating mixing dynamics and their dependence on operating conditions using CFD simulations. Towards this end, fine-grid 3D simulations are conducted for the bubbling fluidization of three distinct Geldart B particles (1.15 mm LLDPE, 0.50 mm glass and 0.29 mm alumina) at superficial gas velocities U/U_{mf}=2-4 in a pilot-scale 50 cm diameter bed. The Two-Fluid Model (TFM) is employed to describe the solids motion efficiently while bubbles are detected and tracked using MS3DATA. Detailed statistics of the flow-field in and around bubbles are computed and used to describe bubble-induced solids micromixing: solids upflow driven in the nose and wake regions while downflow along the bubble walls. Further, within these regions, the hydrodynamics are dependent only on particle and bubble characteristics, and relatively independent of the global operating conditions. Based on this finding, a predictive mechanistic, analytical model is developed which integrates bubble-induced micromixing contributions over their size and spatial distributions to describe the gross solids circulation within the fluidized bed. Finally, it is shown that solids mixing is affected adversely in the presence of gas bypass, or throughflow, particularly in the fluidization of heavier particles. This is because of inefficient gas solids contacting as 30-50% of the superficial gas flow escapes with 2-3$\times$ shorter residence time through the bed. This is one of the first large-scale studies where both the gas (bubble) and solids motion, and their interaction, are investigated in detail and the developed framework is useful for predicting solids mixing in large-scale reactors as well as for analyzing mixing dynamics in complex reactive particulate systems.

Keywords: Gas-solid fluidization, mixing dynamics, bubbling, gas throughflow, solids circulation

1. Introduction

Bubbling fluidized beds have wide applications in the energy and chemical industries because of their high heat and mass transfer rates.[1] Their design and optimization continue to be a challenge because mixing dynamics are particularly sensitive to operating condition while experimental measurements in commercial systems are challenging owing to technical limitations of diagnostics in the harsh conditions these beds often operate in. Computational Fluid Dynamics (CFD) will play a pivotal role in advancing this technology since it enables unrestricted access inside the reactor, enhancing the fundamental understanding of several coupled phenomena and their interactions at various scales.

Solids mixing is critical to ensure high heat transfer and thermal homogeneity in fluidized bed reactors. Despite significant effort over the past few decades, there continues to be a lack of understanding of mixing dynamics, especially at commercial-scales, because (a) most diagnostic techniques are only feasible in small laboratory setups, where the hydrodynamics are significantly affected by the walls[2] and (b) mixing metrics are sensitive to several operating parameters such as bed geometry, superficial gas velocity, particle characteristics and temperature.[3,4,5,6,7,8,9,10] Nevertheless, both experimental[11,12,13,14,15,16] and numerical[2,4,3] studies have concluded that solids mixing is driven by bubble motion through three mechanisms[17,18,19,1] - (a) wake effect- particles get drawn into bubble wakes and accelerate upwards, (b) emulsion drift- particles rain down along bubble walls to replace voids left by rising particles and (c) bubble eruptions- particles are disbursed into the freeboard. Each of these phenomena has been investigated extensively. For instance, experimental visualizations indicate that the area of influence around bubbles experiencing wake lift and emulsion drift is proportional to the bubble size,[16] while the average rise of particles is estimated to be in the range 0.2-$0.5V_b$, where V_b is the bubble rise (axial) velocity.[20,13,14] Meanwhile, the ejection mechanism of solid particles is quite complex and depends on the bubble shape, trajectory as well as near-ejection coalescence events.[19,21,22] This mechanism is also largely responsible for lateral mixing.[10] Overall, these studies enable the fundamental understanding of bubble-particle interactions even though quantitative inferences are often not applicable to commercial operation because (a) isolated bubbles are seldom realized and/or (b) the hydrodynamics in thin lab-scale beds are significantly affected by the front and back walls.

Several frameworks have been proposed for modeling solids mixing in bubbling fluidized beds. The counter-current backmixing model and its derivatives continue to be widely used because they represent circulation mechanistically using *mixing columns* or phases for upflow and downflow.[1,8] Similarly, probabilistic models are based on jump, relaxation and idle times for quantifying the residence of particles within bubble wakes, drift and the dense-phase, respectively.[13,23,24] However, these models are limited by the lack of experimental measurements describing the dynamics within individual phases as well as the exchange coefficients (mass transfer) between them.[20,25] Meanwhile, lateral mixing of particles (both the bed material and *fuel* particles) is commonly represented as a random isotropic dispersion process, despite the convective nature of bubble flow.[26,27] The motion of solids within and across *mixing cells* is characterized using the dispersion coefficient, which is obtained by fitting analytical expressions with tracer measurements.[26] This approach enables quantification of lateral mixing in both downsized and commercial-scale fluidized beds,[9,27,10] even though estimates of the dispersion coefficient may often span several orders of magnitude depending on the bed geometry and operating conditions.[28,29,30] To enhance the predictive capabilities of these models, solids mixing must be correlated with bubbling dynamics, which has not been feasible because of the lack of simultaneous measurements. Towards this end, CFD is a valuable tool because numerical simulations provide unrestricted access inside the reactor. Several studies have investigated mixing using this approach (e.g.[31,15,6,4,32,33]), but most of these employ 2D simulations and, therefore, overestimate mixing rates because resistance to the hydrodynamics from the front and back walls is not accounted for.[3,4] Therefore, in order to understand and quantify mixing in commercial systems, this study employs fine-grid 3D simulations of a large pilot-scale 50 cm fluidized bed so that the hydrodynamics are independent of wall effects.[2]

This work is part of a series of studies investigating bubbling fluidization of Geldart B particles for application to Fluidized Bed Biomass Gasification (FBBG). In,[34,35,36] bubbling dynamics and solids circulation are identified as suitable metrics for characterizing the hydrodynamics accurately. MS3DATA (Multiphase-flow Statistics using 3D Detection and Tracking Algorithm) is developed in[37] for detecting and tracking bubbles, and computes statistics efficiently, using time- and spatially-resolved voidage data from simulations. This algorithm overcomes the inherent limitations of 2D

slice-based statistics which compute inaccurate bubble size and spatial distributions in relatively large ($\sim$20 cm or wider) beds and cannot track bubbles azimuthally. Using these metrics, the effect of reactor size (bed diameter D and initial bed height H_0) on the fluidization hydrodynamics is examined in[2] using fine-grid CFD simulations and it is shown that:

- the mechanism for bubble growth, coalescence and rise is consistent across reactor-scale

- wall independence of the hydrodynamics is achieved only when bubbles are much smaller than bed dimensions

- for bubbling fluidization of Geldart B particles (typically $10^3 < \text{Ar} < 10^5$ and $10^0 < \text{Re} < 10^2$), predictions in a 50 cm diameter bed (and $H_0/D < 1$) are representative of larger scales

Based on these observation, 3D fine-grid simulations are employed in[38] to develop a computational framework for describing the distribution of gas-flow and residence times of different phases. Detailed calculations show that (a) sufficiently far ($\sim$40 particle diameters) from bubbles, conditions in the dense-phase depend only on the particle properties ($\varepsilon_{\text{mf}}, U_{\text{mf}}$), (b) bubble rise is proportional to the square root of its diameter even though it could be affected significantly by the presence of walls or neighboring bubbles, and (c) gas throughflow increases in areas of high solids permeability and as much as 30-50% of the superficial gas flow could bypass the bed with 2-3$\times$ shorter residence time.

The objectives of this study are two-fold: the fundamental investigation of bubble-induced solids mixing mechanism and the development of a mechanistic model for correlating solids circulation with bubbling dynamics. Towards this end, fine-grid 3D simulations are conducted for the bubbling fluidization of three distinct Geldart B particles (alumina, glass and LLDPE with Archimedes numbers 1021, 10582 and 41161, respectively) at superficial gas velocities U/U_{mf}=2-4 in a 50 cm diameter bed to ensure predictions are representative of larger scales. A brief description of the simulation setup and tools is first discussed in Section 2. For all cases, the distribution of gas-flow and its relevance to solids mixing are discussed in Section 3.1. Next, solids micromixing around bubbles is investigated in Section 3.2 and based on quantitative insights from these calculations, a mechanistic model for reactor-scale solids mixing is developed in Section 3.3. All simulations are performed using MFiX (Multiphase Flow with Interface eXchanges), an open-source code developed at the National Energy Technology Laboratory, USA to describe the hydrodynamics of solid-gas systems. Bubble detection, tracking and related post-processing are performed using MS3DATA.[37]

2. Simulation Setup

The simulation setup employed in this study is presented and validated in.[36,2] Key aspects regarding the simulation setup are discussed below.

2.1. Governing Equations

Simulations are based on the Two-Fluid Model (TFM) framework which represents the solids phase as a continuum and optimally balances fidelity with computational needs at large-scales. For cold fluidization, the transport equations for mass and momentum reduce to

$$\frac{\partial}{\partial t}\left(\varepsilon_k \rho_k\right) + \nabla \cdot \left(\varepsilon_k \rho_k \mathbf{V}_k\right) = 0 \tag{1}$$

$$\frac{\partial}{\partial t}\left(\varepsilon_k \rho_k \mathbf{V}_k\right) + \nabla \cdot \left(\varepsilon_k \rho_k \mathbf{V}_k \mathbf{V}_k\right) = \nabla \cdot \mathbf{S}_k - \varepsilon_k \nabla P_g + \varepsilon_k \rho_k \mathbf{g} + \left(\delta_{km}\mathbf{F}_{gm} - \delta_{kg}\mathbf{F}_{gm}\right) \tag{2}$$

$$\delta_{ki} = \begin{cases} 1 & \text{if } k = i \\ 0 & \text{otherwise} \end{cases}$$

where ε, ρ and $\mathbf{V}$ are the volume fraction, density and velocity for the gas ($k = g$) and solid ($k = m$) phases. The solids stress tensor $\mathbf{S}_m$ is dependent on the particle properties and local flow conditions (solids packing and velocity fields), and is evaluated using the Kinetic Theory of Granular Flow (KTGF)[39] alongwith the frictional contribution in dense pockets of the bed.[40] $\mathbf{I}_{gm}$ represents the gas-solids drag force and is reasonably described using the Gidaspow model at low superficial gas velocities ($U/U_{mf} < 4$).[41,36] Finally, the system of equations is closed by solving the transport equation for granular temperature Θ_m which represents the kinetic energy associated with the fluctuating component of particle velocity and is governed by

$$\frac{3}{2}\left(\frac{\partial(\varepsilon_m\rho_m\Theta_m)}{\partial t} + \nabla\cdot(\varepsilon_m\rho_m\mathbf{V}_m\Theta_m)\right) = \boldsymbol{S}_m:\nabla\mathbf{V}_m + \nabla\cdot\mathbf{q}_{\Theta_m} - \gamma_{\Theta_m} + \phi_{gm} \tag{3}$$

considering production $\mathbf{S}_m:\nabla\mathbf{V}_m$, diffusion $\nabla\cdot\mathbf{q}_{\Theta_m}$ and dissipation through particle-particle γ_{Θ_m} and particle-gas interactions ϕ_{gm}. Further details regarding the physical model and governing equations can be found in[2] (and citations therein).

2.2. Boundary Conditions

The wall boundary condition is specified as no-slip for the gas-phase and partial slip for the solids velocity $\mathbf{V}_{sl}$ computed using the Johnson-Jackson model.[42] This model is based on the simultaneous conservation of solids momentum and granular energy at the walls and depends on the mechanical parameters: (a) particle-wall restitution coefficient e_w and (b) specularity coefficient ϕ_w characterizing the loss in particle normal and tangential momenta on wall collisions, respectively. Detailed comparison of simulations with experimental measurements[35,36] shows that the choice of ϕ_w is critical, especially while simulating lab-scale beds, and is quantified *in situ* using the Li-Benyahia model.[43] Meanwhile, the choice of cylindrical coordinates requires numerical boundary conditions at the grid centerline: i.e. the centerline radial velocity is predicted using the surrounding flow field. This prevents the spurious accumulation of solids.[34] Finally, uniform gas velocity is imposed at the distributor even though distributor design effects are well-documented.[44,45,10] Although the distribution of gas-flow is idealized, this assumption should not influence the solids modeling framework which accounts for the bubble size and spatial distributions implicitly (later discussed in Section 3.3).

2.3. Numerical Approach

All simulations are performed using MFiX, an open-source code developed at the National Energy Technology Lab (NETL). The governing equations are solved using the SIMPLE (Semi-Implicit Method for Pressure Linked Equations) algorithm which uses a predictor-corrector approach to establish a conservative field- variables are solved using the established pressure field in the finite volume framework and subsequently corrected using gas and solids continuity equations. Grid cells for all simulations are in the range 8-10 particle diameters to ensure accuracy without breaking down the solids continuum assumption.[34] The forward Euler approach is used for time marching with a variable time step to maintain numerical stability; typically in the range 10^{-6} s to 10^{-4} s. More details regarding the numerical algorithm can be found in.[46]

2.4. Bubble Statistics

Bubble statistics are quantified using MS3DATA (Multiphase-flow Statistics in 3D using Detection And Tracking Algorithm),[37] which is developed in-house for accurate and scalable post-processing of 3D simulation data. Using this tool, time- and spatially-resolved voidage data from simulations is first sampled at 100 Hz for 20s (2000 frames in total), discounting the first 10s for transient startup effects. Next, bubbles are detected by thresholding data and linking neighboring cells using a sweeping algorithm. Finally, properties are computed by aggregating cells associated with each bubble and rise velocities by linking bubbles based on their lateral and axial locations. This tool also enables the

Table 1: Summary of operating conditions

D [cm]	50		
H_0 [cm]	50		
U/U_{mf}	2-4		
Particles	Alumina	Glass	LLDPE
d_p [mm]	0.29	0.50	1.15
ρ_s [kg/m^3]	1250	2500	800
U_{mf} [m/s]	0.04	0.18	0.24
Ar [$\times 10^3$]	1.02	10.58	41.16

computation of detailed statistics of the flow-field (e.g. velocities, pressure, granular temp etc) in and around bubbles.

3. Results and Discussion

Mixing dynamics are analyzed using 3D simulations for the bubbling fluidization of 0.29 mm alumina, 0.50 mm glass and 1.15 mm LLDPE particles in a 50 cm diameter fluidized bed. These conditions are summarized in Table 1. The minimum fluidization velocity U_{mf} for these particles has been obtained experimentally[47, 48] and the operating conditions are representative of larger reactors because bubbles are small compared to bed dimensions[2]. Grid resolution and validation studies can be found in[36, 2] while MS3DATA[37] is employed to isolate bubbles and compute detailed statistics of the solids motion around them. Bubble contours are defined using the void fraction threshold $\varepsilon_{gb} = 0.7$, and only the dense-phase or *emulsion* (i.e. all areas with $\varepsilon_s > 1 - \varepsilon_{gb}$) is considered for the statistical description of solids flow. This is reasonable considering that under typical bubbling conditions, more than 95% of solids momentum is within the dense-phase (verified for all simulations but not shown here for brevity) and the contribution from within bubbles to the overall particle mixing may be neglected. In the following sections, the distribution of gas-flow and residence times, and their impact on solids mixing, are first discussed in Section 3.1. Next, solids micromixing around individual bubbles is investigated in Section 3.2 followed by the development of a mechanistic model for predicting reactor-scale solids mixing in Section 3.3.

3.1. Gas-flow distribution and relevance to mixing

Instantaneous visualizations from the fluidization of LLDPE particles at U/U_{mf}=2 are presented in Figure 1 and show that small bubbles are formed at the distributor and rise laterally inwards as they grow and coalesce. This pattern is consistent across scales and the critical height at which most bubbles reach the center and rise vertically thereafter is related to the bed diameter and operating conditions.[2] In,[38] detailed statistics of the gas flow in and around bubbles were computed and it was established that

- dense phase conditions sufficiently far from bubbles ($\sim 30 d_p$) are dependent largely on the particle properties (minimum fluidization conditions). This is also shown in Figure 2 where $2\times$ increase in the superficial gas flow results only in 10% increase in the average dense-phase gas velocity.

- visible bubble flow is related to the bubble size and spatial distributions ($V_b \propto \sqrt{D_b}$).
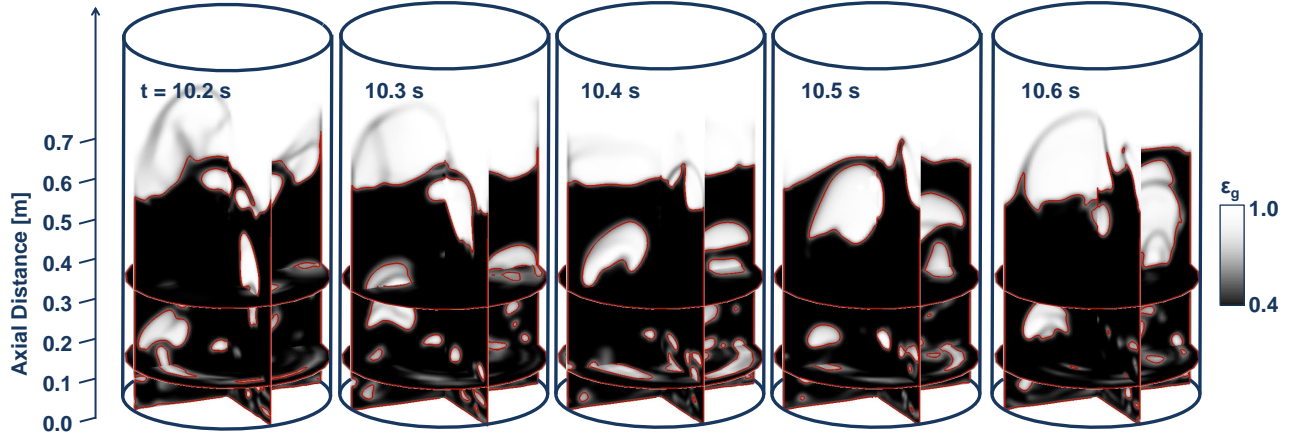
5

Figure 1: Instantaneous visualizations of void fraction in the fluidization of LLDPE particles at U/U$_{\mathrm{mf}}$=2 in a 50 cm diameter bed. Red colored contour lines indicate bubbles ($\varepsilon_g = 0.7$).
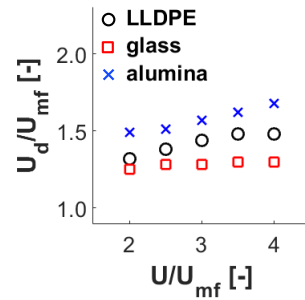

Figure 2: Time and spatially averaged dense phase gas velocity in the fluidization of LLDPE, glass and alumina particles at U/U$_{\mathrm{mf}}$=2-4 in a 50 cm diameter bed.

- voidage distribution around bubbles increases the local permeability of the dense phase which results in (a) preferential bubble pathways, as bubbles are propelled towards areas already frequented by bubbles (*gulf-stream* circulations) and (b) throughflow, as low resistance networks are established for interstitial gas to escape.

Gas distribution statistics from the fluidization of 1.15 mm LLDPE, 0.50 mm glass and 0.29 mm alumina particles in a 50 cm diameter bed are presented in Figure 3. As U/U$_{\mathrm{mf}}$ is raised from 2 to 4, dense-phase gas composition decreases (approximately from 75% to 40% for alumina particles and 60% to 25% for the other two) because of more bubbles formed close to the distributor which rise, grow and coalesce to form larger ones. This decrease is compensated by the increase in visible bubble flow for the lighter alumina particles, in stark contrast to the fluidization of heavier glass and LLDPE particles where almost 2× increase in throughflow is observed. The tendency for throughflow can be quantified using the γ factor:[49]

$$\gamma = \frac{\chi_b}{1 - \chi_d} \tag{4}$$

where χ_b and χ_d are the gas volume fractions in the visible bubble and dense phase, respectively. γ factors for all cases are presented in Figure 4. Fluidization of alumina particles shows high γ factor ≈ 0.8 indicating that most of the excess gas rises as bubbles, whereas $\gamma \approx 0.3$-0.4 for the heavier particles indicating higher tendency for throughflow. These observations are consistent with previous measurements in lab-scale bubbling fluidized beds.[49]
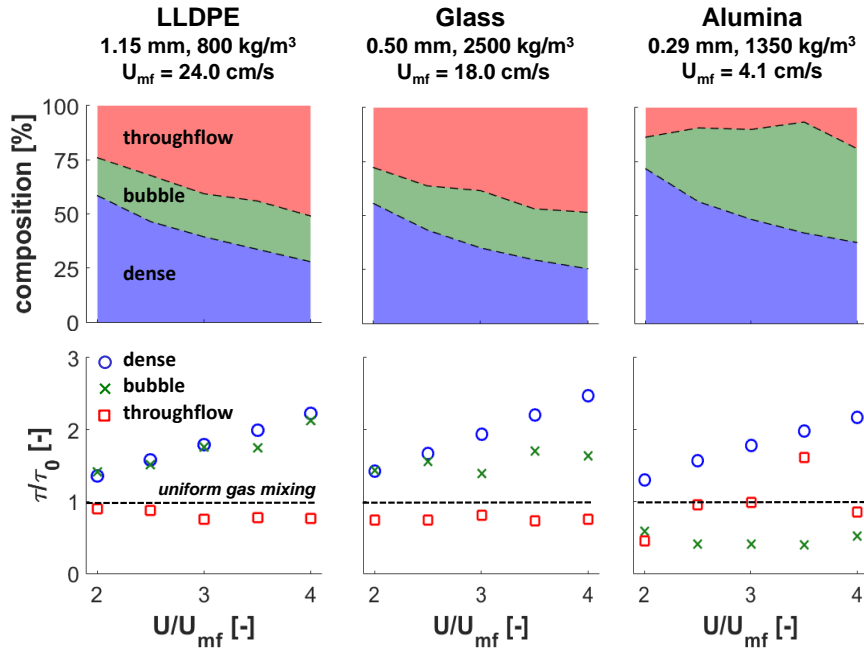
Figure 3: Gas-flow composition and residence time distribution for the dense, visible bubble and throughflow phases in the fluidization of LLDPE, glass and alumina particles at U/U_{mf}=2-4 in a 50 cm diameter bed.
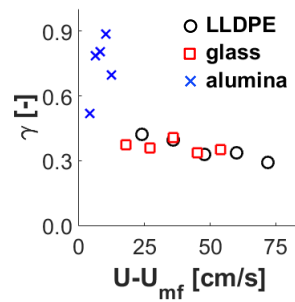

Figure 4: Throughflow factor γ in the fluidization of LLDPE, glass and alumina particles at U/U_{mf}=2-4 in a 50 cm diameter bed (Equation 4)

.

Meanwhile, Figure 3 also shows the residence time of gas flow through each phase, normalized by $\tau_0 = H_0\varepsilon_0/U$ which is the residence time of the superficial gas flow through the bed assuming homogeneous distribution. While the dense-phase residence time τ_d is relatively unaffected by superficial gas flow,[38] τ_d/τ_0 increases at higher U/U_{mf} because of the decrease in τ_0. Similarly, τ_b is the average residence time of bubbles in the reactor. In the fluidization of alumina particles, it is evident that bubbles are much faster (2-4×) than the dense-phase gas flow, unlike the fluidization of heavier particles. This is indicative of the *fast-bubbling* which has been observed in the bubbling fluidization of Geldart A particles,[49] and is not surprising here because alumina particles are located at the lower end of the Geldart B spectrum. For glass and LLDPE particles, τ_{tf}/τ_0 is relatively constant (≈ 0.9) indicating that the residence time for throughflow decreases (proportionally) as τ_0 decreases at higher U/U_{mf}. Overall, gas mixing quality can be characterized by (a) throughflow composition χ_{tf} and (b) disparity in time-scales between the dense and throughflow phases τ_d/τ_{tf}. Figures 3 and 4 clearly demonstrate that higher superficial gas flow increases the inhomogeneity in gas mixing because of increasing (and faster) throughflow.

Figure 5 illustrates the dependence of solids mixing on superficial gas flow (U/U_{mf}= 2-4) in the bubbling fluidization of all particles. τ_c^+ is the positive circulation time (computed using Equation 21 and discussed in detail later) and represents the average time for particles to traverse the bed height from the gas distributor. Figure 5a shows that for all particles, τ_c^+ decreases as excess gas velocity is increased because solids mixing is driven by bubble rise, growth and coalescence activity, all of which increase at higher $U-U_{mf}$. The rate of decrease, however, reduces at higher gas velocities because of increasing gas bypass through bubbles. The adverse implications of throughflow are better realized by non-dimensionalizing the gas flow and mixing time-scales using the particle relaxation time τ_p to yield the Stokes numbers:

$$\text{Stk}_g = \frac{\tau_p}{\tau_0} = \frac{U}{\varepsilon_0 H_0} \frac{\rho d_p^2}{18\mu_g} \qquad \text{Stk}_c^+ = \frac{\tau_p}{\tau_c^+} = \frac{1}{\tau_c^+} \frac{\rho d_p^2}{18\mu_g} \tag{5}$$

so that Stk_g and Stk_c^+ are representative of the superficial gas flow and average solids velocity in the bed, respectively. Figure 5b shows that for heavier LLDPE and glass particles, (a) $\text{Stk}_c^+ << \text{Stk}_g$, unlike the case of lighter alumina particles where these time-scales are comparable, and (b) Stk_c^+ does not increase linearly with Stk_g (in fact $\text{Stk}_c^+ \propto \text{Stk}_g^{0.85}$), i.e. increasing the superficial gas flow does not translate to a proportional raise in the average solids velocity. This is because at higher U/U_{mf}, a large fraction of the added gas constitutes throughflow and bypasses the bed with 2-3× shorter residence time. Thus, the resulting gas-solids contacting is inefficient and improvements in mixing rate (or decrease in mixing times) are underwhelming. While the coupling of gas and solids mixing dynamics is explained in detail in the following sections, Figure 5 clearly demonstrates the contribution of throughflow towards sub-optimal solids mixing and highlights the need for more homogeneous gas-flow distribution through efficient reactor and distributor designs.

3.2. Bubble-induced micromixing

For the instantaneous voidage visualizations in Figure 1, Figure 6 presents the solids axial velocity fields. It is evident that solids upflow is collocated with the presence of bubbles. This corroborates that solids circulation is driven by bubbles and further highlights the need for a better understanding of solids micromixing around individual bubbles.

Figure 7 shows typical bubbles observed in the fluidization of LLDPE particles at U/U_{mf}=2 and the solids velocity field around them. Despite considerable differences in their sizes and shapes, solid particles generally rise along the bubble axis and rain down along the edges. For these bubbles,
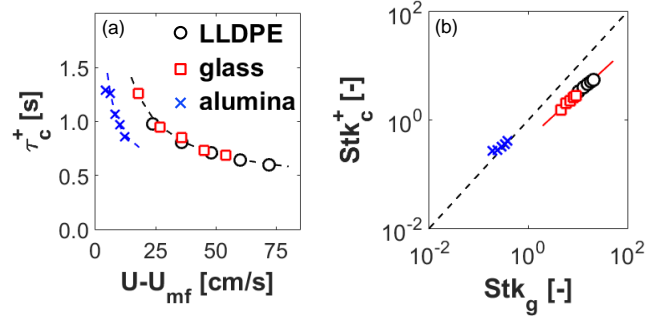
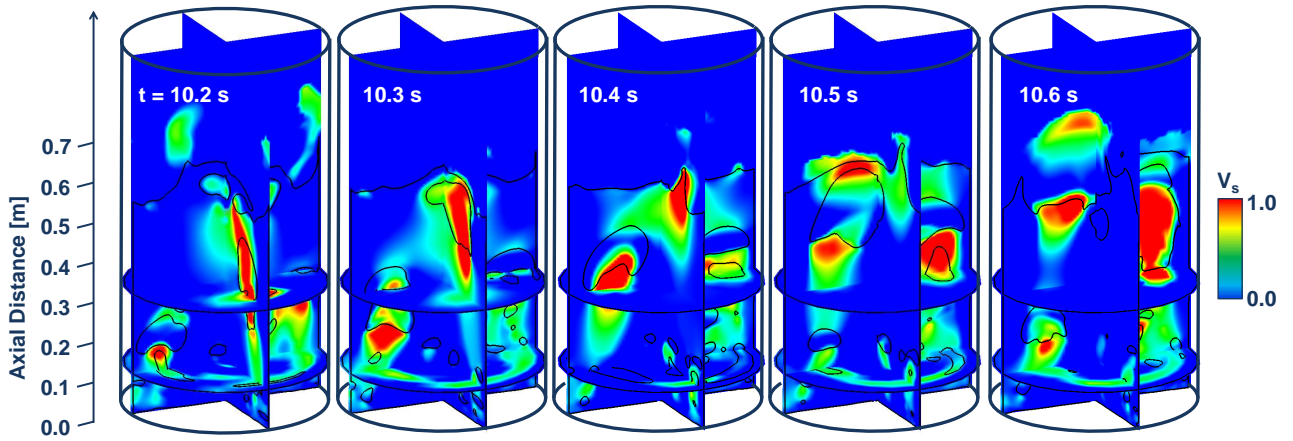Figure 5: Dependence of solids mixing on particle properties and superficial gas flow in a 50 cm diameter bed.

Figure 6: Solids axial velocity for void fraction visualizations presented in Figure 1. Black colored contour lines indicate bubbles ($\varepsilon_g = 0.7$).
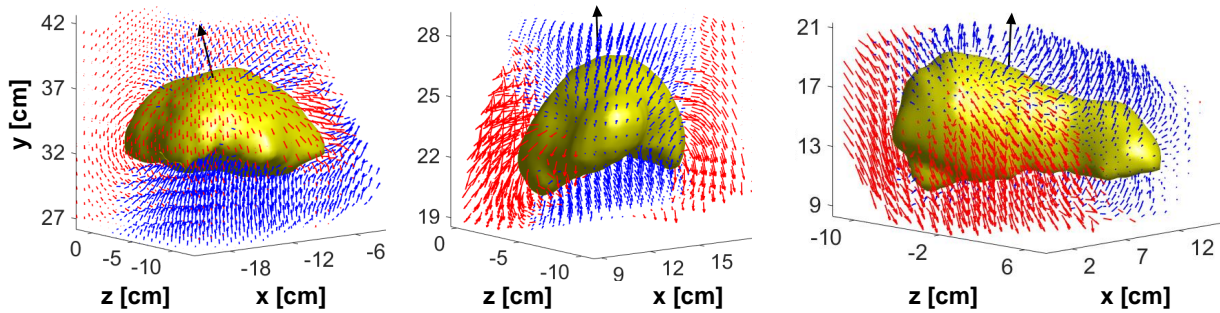

Figure 7: Solids velocity field (blue - upwards, red - downwards) around typical bubbles (velocity vector indicated in black) in the fluidization of LLDPE particles at $U/U_{mf}=2$ in a 50 cm diameter bed (vector lengths may only be used as estimates)
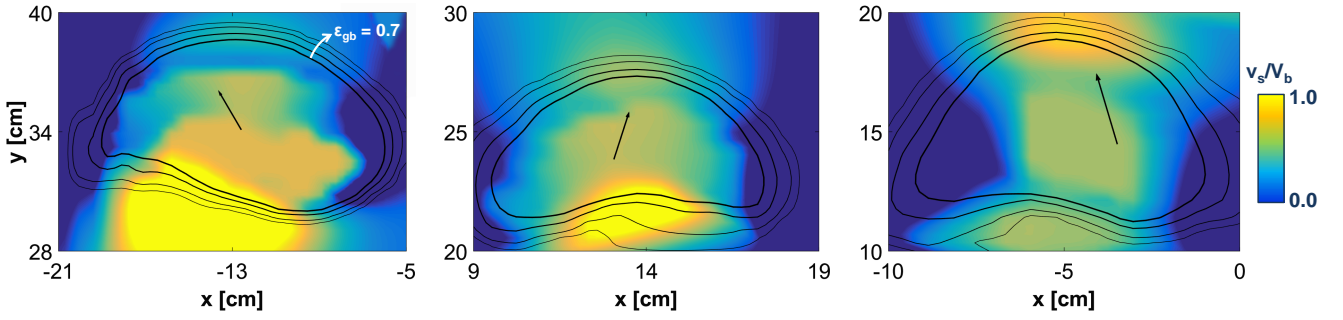
9

Figure 8: Solids axial velocity field (normalized by bubble axial velocity) in and around bubbles presented in Figure 7. Black colored contours indicate voidage (outwards)- 0.70, 0.60, 0.50 and 0.45.

Figure 8 presents 2D solids velocity data along a vertical slice through their centroids. Consistent with experimental evidence in thin rectangular beds (e.g.[17,50]), the highest magnitudes are observed in the nose and wake regions around every bubble. However, since bubbles are rarely symmetric and the idealized spherical-cap shape is seldom realized under typical operating conditions, defining different regions around bubbles is non trivial. For this purpose, emulsion points E_{ij} ($\mathbf{x_{ij}}$) in the neighborhood of bubble b_j are segregated based on the angle α_{ij} subtended with the bubble axis (velocity vector $\mathbf{V_{b,j}}$ through centroid $\mathbf{C_j}$), i.e.

$$\alpha_{ij} = cos^{-1}\left(\frac{\mathbf{V_{b,j}} \cdot (\mathbf{x_{ij}} - \mathbf{C_j})}{|\mathbf{V_{b,j}}||\mathbf{x_{ij}} - \mathbf{C_j}|}\right) \tag{6}$$

Similarly, the distance r_{ij} from the bubble boundary is computed by minimizing the distance of E_{ij} from all cells constituting the bubble boundary Ω_j (with cell centers $\mathbf{x}_{\Omega_j}$) i.e.

$$r_{ij} = \min_{\Omega_j}|\mathbf{x_{ij}} - \mathbf{x}_{\Omega_j}| \tag{7}$$

Subsequently, the nose and wake regions are defined as areas within the conical angles $\alpha \in [0, \pi/6]$ and $\alpha \in [5\pi/6, \pi]$, respectively. Note that there is no distinct transition between different regions and the choice of demarcating angles is somewhat arbitrary.

Detailed statistics of the flow-field around approximately 100 linked bubbles (from 15 randomly selected frames) are computed for every operating condition, after filtering out bubbles in close proximity to the walls and/or comparable to bed dimensions in order to remove wall effects. For the fluidization of glass particles at U/U_{mf}=2 and 3, Figure 9 shows that the average solids concentration ε_s increases exponentially from the bubble boundary (at $\varepsilon_s = 1 - \varepsilon_{gb}$) to the dense-phase which is minimally fluidized ($\varepsilon_{s,mf} \approx 0.6$) within 40 particle diameters. Meanwhile, the average solids axial velocity in the nose ($\alpha \in [0, \pi/6]$) and wake regions ($\alpha \in [5\pi/6, \pi]$) is in the range 0.4-0.6V_b and decreases further away from the bubble boundary because of increasing frictional dissipation as the solids packing fraction increases. On the other hand, towards the lateral edges of bubbles ($\alpha \in [\pi/6, 5\pi/6]$), v_s is relatively much lower (or negative) indicating significant downflow in these areas. Note that the average solids axial velocity is mass-weighted and computed using

$$\bar{v}_s(r) = \frac{\int\limits_{\psi} \varepsilon_s v_s \, dA}{\int\limits_{\psi} \varepsilon_s \, dA} \tag{8}$$

where the integration area ψ encompasses all cells E_{ij} such that $r - \Delta r/2 \leq r_{ij} \leq r + \Delta r/2$.
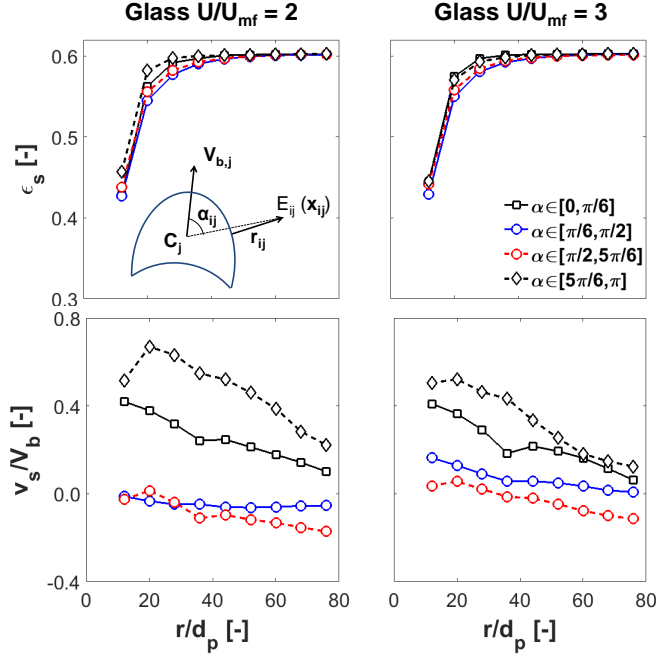
10

Figure 9: Average solids distribution and axial velocity in different regions around a bubble in the fluidization of glass particles at U/U$_{\mathrm{mf}}$=2 and 3. r is the distance from the bubble boundary while α and v_s are computed using Equations 6 and 8, respectively.

3.2.1. Nose and wake regions

Similar to Equation 8, upflow statistics in the nose and wake regions are quantified using

$$\bar{v}_s^+(r) = \frac{\int\limits_{\psi} \varepsilon_s v_s \, dA^+}{\int\limits_{\psi} \varepsilon_s \, dA^+} \qquad dA^+ = \begin{cases} dA & \text{if } v_s(\mathbf{x}, t) > 0 \\ 0 & \text{otherwise} \end{cases} \tag{9}$$

For bubbles observed in the fluidization of LLDPE and glass particles, these statistics are presented in Figure 10. Consistent with observations in Figure 9, $\bar{v}_s^+$ is highest close to the bubble boundary ($\sim 0.6V_b$) and decreases further away. Interestingly, both the distribution and velocity profiles are relatively independent of U/U$_{\mathrm{mf}}$ (also true for other cases not shown here for brevity), suggesting that bubble-induced micromixing is dependent only on the particle and bubble (velocity) characteristics. Note that the distance r from the bubble boundary is normalized using the particle diameter d_p, instead of the volume-based bubble diameter D$_b$ because (a) most bubbles are deformed with typical aspect ratios in the range 0.2-1.5 and (b) statistics show relatively weak dependence on the bubble size, as also presented in Figure 11 for the fluidization of LLDPE and glass particles at U/U$_{\mathrm{mf}}$=2. Overall, observations in Figure 10 suggest that solids circulation is related to the bubbling dynamics, which in turn are affected by superficial gas flow, particle properties and other operating conditions. This interplay between the gas and solids motion is discussed in detail below.

3.3. Mechanistic model for reactor-scale mixing

Efficient solids mixing is critical for maintaining thermal and concentration homogeneity in flu-idized bed reactors. However, direct solids measurements in large-scale reactors and/or operating in harsh environments is often prohibitive making design and performance optimization challenging. In this regard, correlating solids mixing with bubbling dynamics (and the overall gas-flow distribution) is
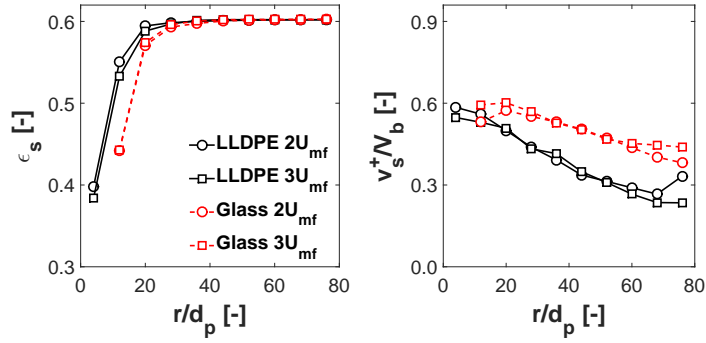
11

Figure 10: Average solids distribution and axial velocity in the nose ($\alpha \leq \pi/6$) and wake ($\alpha \geq 5\pi/6$) regions around a bubble in the fluidization of glass and LLDPE particles at U/U$_{\mathrm{mf}}$=2 and 3. r is the distance from bubble boundary and $\bar{v}_s^+$ is computed using Equation 9.
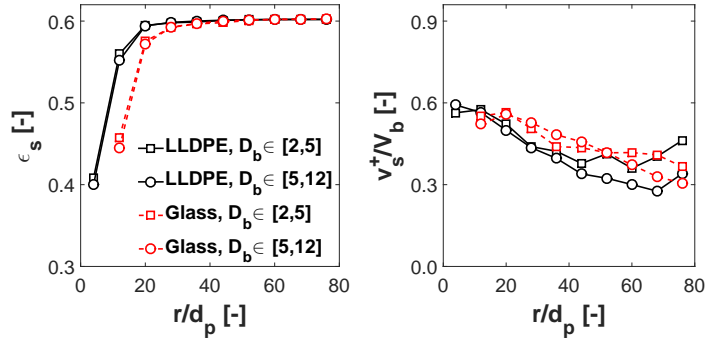

Figure 11: Average solids distribution and axial velocity in the nose ($\alpha \leq \pi/6$) and wake ($\alpha \geq 5\pi/6$) regions around a bubble in the fluidization of glass and LLDPE particles at U/U$_{\mathrm{mf}}$=2. Statistics are segregated based on bubble size (diameter D$_{\mathrm{b}}$)- small bubbles in the range 2-5 cm and large bubbles in the range 5-12 cm. r is the distance from bubble boundary and $\bar{v}_s^+$ is computed using Equation 9.

extremely beneficial but is often not possible because of technical challenges in the simultaneous measurements of gas and solids motion. As highlighted in Section 3.2, this is not the case with numerical simulations which allow unrestricted access into any region of interest within the reactor. Therefore, in this section, quantitative insights derived from detailed calculations of the solids flow-field around bubbles are employed to develop an analytical, mechanistic model for predicting the overall solids mixing.

Reactor-scale solids circulation is quantified by integrating bubble-induced micromixing contributions over their size and spatial distribution. Based on observations in[38] and Section 3.2, the following relations are employed (discussed in detail for upflow, but extended to downflow later):

- Bubble velocity is proportional to $\sqrt{gD_b}$[38] through the correlation coefficient c_1, where D_b is the bubble diameter i.e.

$$V_b = c_1 \left(0.71 \sqrt{gD_b} \right) \tag{10}$$

- Solids distribution and momentum around a bubble depend only on its characteristics through coefficients c_{2a} and c_{2b}:

$$\langle \varepsilon_s^+ \rangle = c_{2a}\, \varepsilon_{s,max} \qquad \langle \varepsilon_s^+ v_s^+ \rangle = c_{2b}\, \varepsilon_{s,max} V_b \tag{11}$$

Note that $\langle \rangle$ indicates spatial averaging within the region of influence around a bubble and is discussed later. Based on the assumption that the projected area for solids upflow is the bubble cross-sectional area A_b (which is reasonable considering that most solids upflow is within the nose and wake regions), the positive circulation flux is

$$J_c^+ = \sum \rho_s \langle \varepsilon_s^+ v_s^+ \rangle A_b / \sum A_b \tag{12}$$

where the summation is performed over all bubbles within the reactor section of interest. Therefore, the average positive solids velocity is

$$\langle v_s^+ \rangle = \frac{J_c^+}{\rho_s \langle \varepsilon_s^+ \rangle} = \frac{1}{\langle \varepsilon_s^+ \rangle} \frac{\sum \langle \varepsilon_s^+ v_s^+ \rangle A_b}{\sum A_b} \tag{13}$$

Equation 13 can be simplified using Equations 10-11 alongwith the assumption of spherical bubbles, so that:

$$\langle v_s^+ \rangle = c_1 c_2\, 0.71 \sqrt{g \bar{D}_{bv}} \tag{14}$$

$$\bar{D}_{bv} = \left(\sum D_b^{2.5} / \sum D_b^2 \right)^2 \tag{15}$$

where $\bar{D}_{bv}$ is the axial velocity-based average bubble diameter. c_1 captures the influence of operating conditions and the *momentum transfer* coefficient $c_2 = c_{2b}/c_{2a}$ quantifies the momentum imparted by a bubble onto the surrounding dense-phase. Using Equation 14, the positive circulation time τ_c^+ is, therefore, given by

$$\tau_{c,bub}^+ = \frac{H_0}{\langle v_s^+ \rangle} = \frac{H_0}{c_1 c_2\, 0.71 \sqrt{g \bar{D}_{bv}}} \tag{16}$$

Using a similar methodology, solids downflow along the bubble boundaries can also be quantified and the total circulation time τ_c is

$$\tau_{c,bub} = \tau_{c,bub}^+ + \tau_{c,bub}^- = \frac{H_0}{\left[c_1\, 0.71 \sqrt{g \bar{D}_{bv}} \right]} \left(\frac{1}{c_2} + \frac{1}{c_3} \right) \tag{17}$$

13

Circulation time is the average time taken by particles to complete one turnover in the bed i.e. to traverse the bed height from the distributor and back. Equation 17 shows that $\tau_{c,bub}$ depends on the bubbling dynamics (term within [ ]), and momentum transfer coefficients c_2 and c_3 for upflow and downflow, respectively. The latter are quantified by spatial averaging within the region of influence around a bubble, as discussed below.

Region of influence around a bubble

Spatial averaging for quantifying the momentum transfer coefficients requires identification of the region of influence around a bubble. For fluidized beds operating at low superficial gas velocities (typically $< 1.5 U_{\mathrm{mf}}$), this is relatively trivial because dense-phase perturbations asymptotically converge to 0 (damped) sufficiently far from the bubble. However, under more realistic operating conditions, bubbles rise seldom in isolation and surrounding solids flow is affected by the presence and interaction of neighboring bubbles. Therefore, to quantify solids micromixing induced by a rising bubble, the region of influence around a bubble is identified by considering the ratio of particle inertia and convective (bubble) time-scales, i.e. the inertial number:

$$I = \frac{\text{particle inertia time}}{\text{convective time}} = \frac{d_p}{\sqrt{P_s/\rho_s}} \frac{V_b}{r} \tag{18}$$

where d_p is the particle diameter, P_s is the solids pressure and r is the distance from the bubble boundary. Similar to the Bagnold number which is popularly used in granular shear flow for defining constitutive relations,[51] the physical interpretation of I is that particles moves under the convective influence of a bubble (macroscale deformation), until they are pushed back by the confining pressure P_s. The time-scale for this microscale deformation (inertia time) is estimated as $\left(d_p/\sqrt{P_s/\rho_s} \right)$ by assuming the free-fall of a particle under pressure P_s over distance d_p. Using the kinetic theory of granular flow,[41]

$$P_s = \rho_s \theta_s \left(1 + 2 \left(1 + e \right) g_0 \varepsilon_s \right) \tag{19}$$

$$g_0 = \left(1 - \left(\frac{\varepsilon_s}{\varepsilon_{s,max}} \right)^{1/3} \right)^{-1}$$

where g_0 is the radial distribution function and e is the inter-particle restitution coefficient. Since $\theta_s \sim v_s^2$,[41] Equation 18 can be simplified to

$$I \sim \frac{d_p}{r} \frac{V_b}{v_s} \frac{1}{\sqrt{1 + 2 \left(1 + e \right) g_0 \varepsilon_s}} \tag{20}$$

so that the inertial number I is related to the normalized distance from the bubble boundary r/d_p, normalized solids axial velocity v_s/V_b and local solids concentration ε_s. Figure 12 shows the inertial number profile, averaged around approximately 100 bubbles, for the fluidization of different particles. Close to the bubble boundary (i.e. for very small r), I is relatively high valued because the convective time-scale (for bubble motion) is very short; in fact Equation 20 suggests that $I \to \infty$ as $r \to 0$ which is not realized in Figure 12 because r is limited by the grid resolution of CFD simulations. On the other hand, far from the bubble boundary, $I \to 0$ as particles are densely packed (see Figure 10a) resulting in high solids pressure. In fact, beyond 40 particle diameters, I is over-predicted because Equation 20 does not account for frictional pressure, which is expected to be dominant as $\varepsilon_s \to \varepsilon_{s,mf}$. Overall, based on observations in Figure 12, it is evident that convective solids mixing is induced by bubbles only within short distances ($\sim 30 d_p$), while significantly slower bulk mixing (far from bubbles) is driven by microscale deformations (inter-particle interactions). Thus, momentum transfer coefficients c_2 and c_3 in Equation 17 are computed by spatially averaging the solids distribution and
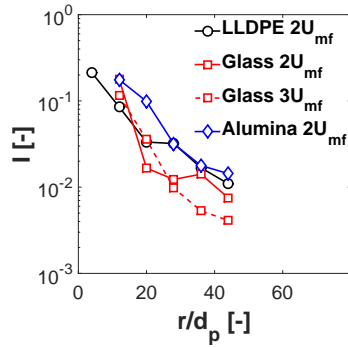
Figure 12: Average inertial number I around a bubble in the fluidization of LLDPE, glass and alumina particles. r is the distance from bubble boundary and I is computed using Equation 20.
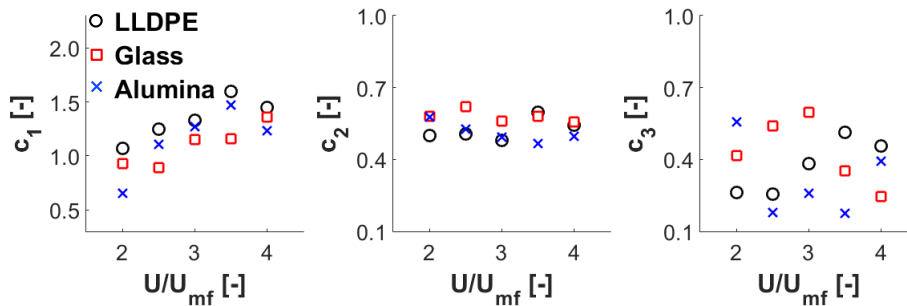

Figure 13: Coefficients for reactor-scale mixing model in Section 3.3

axial velocity fields within r/d_p=30 around bubbles (using Equation 11).

Model verification

For all cases, coefficients c_1, c_2 and c_3 are presented in Figure 13. c_1 is the coefficient for linear regression (bubble diameter-axial velocity correlation, Equation 10) and generally increases with superficial gas velocity indicating that similar sized bubbles rise faster at higher U/U_{mf}. Momentum transfer coefficients c_2 and c_3 are computed using Equation 11 by filtering solids flow-field data based on the direction of solids motion (+ upwards, − downwards) and averaging within $30d_p$ from the bubble boundaries. c_2 is approximately constant (in the range 0.4-0.6), consistent with the hypothesis that bubble-induced solids upflow is dependent only on the bubble characteristics (and independent of the superficial gas flow). Note that this range is higher than 0.2-0.5 estimates reported in[20,13,14] where experiments were conducted in lab-scale/thin-rectangular fluidized beds and the hydrodynamics are considerably slower because of wall resistance to the flow.[36,2] Moreover, bubble velocities in these studies (and others which investigate solids mixing) are often predicted based on empirical correlations because of the complexity of simultaneous gas and solids flow measurements. This is, however, not the case with numerical simulations which enable detailed insights into the hydrodynamics. On the other hand, there is considerable scatter and no obvious dependence of c_3 on U/U_{mf}. Unlike solids upflow which depends largely on the bubble characteristics, solids downflow along the lateral edges is strongly influenced by the presence of neighboring bubbles and/or retardation effects in the proximity of walls. In order to realize the dependence of c_3 on bubble characteristics and/or U/U_{mf}, these effects must be decoupled by explicitly accounting for the bubble location (distance from wall boundary) and local bubble frequency in Equations 10-11. This will be analyzed in future publications. Nevertheless, using these coefficients, circulation time is estimated from bubble statistics using Equations 16-17 and
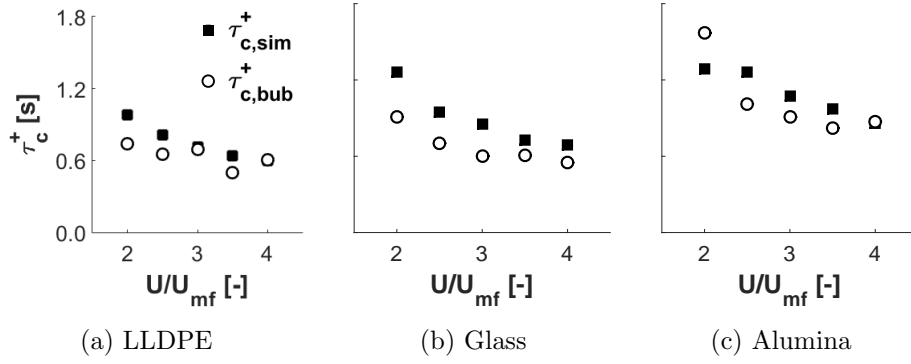
15

Figure 14: Comparison of average positive circulation time estimated from bubbling dynamics $\tau^+_{c,bub}$ using Equation 16 with $\tau^+_{c,sim}$ predictions directly from simulation data using Equation 21.

compared with predictions from simulation data directly using

$$\tau_{c,sim} = \tau^+_{c,sim} + \tau^-_{c,sim} \tag{21}$$

$$= \int\limits_0^{H_0} \frac{dy}{\bar{v}^+_{s,sim}(y)} + \int\limits_0^{H_0} \frac{dy}{\bar{v}^-_{s,sim}(y)}$$

$$\bar{v}^+_{s,sim}(y) = \left\langle \frac{\iint \varepsilon_s(\mathbf{x},t)\, v_s(\mathbf{x},t)\, dA^+}{\iint \varepsilon_s(\mathbf{x},t)\, dA^+} \right\rangle$$

$$dA^+ = \begin{cases} dA & \text{if } v_s(\mathbf{x},t) > 0 \\ 0 & \text{otherwise} \end{cases}$$

and similarly $\bar{v}^-_{s,sim}$ for downflow. Figure 14 shows $\tau^+_{c,bub}$ estimated using Equation 16 and $\tau^+_{c,sim}$ predicted from simulation data using Equation 21 for the bubbling fluidization of all three particles at U/U$_{mf}$=2-4. In general, circulation time decreases as U/U$_{mf}$ is increased because of higher bubble activity driving faster solids circulation. Comparison of $\tau^+_{c,bub}$ and $\tau^+_{c,sim}$ indicates excellent agreement-the average error $\approx$ 15% is reasonable considering the simplicity of the model ($\tau^+_{c,bub}$) for capturing the complex hydrodynamics. On the other hand, $\tau_{c,bub}$ shows larger deviations from $\tau_{c,sim}$ in Figure 15 because Equation 17 does not account for wall resistance. These effects become increasingly prominent when bubbles are large (i.e. bed has transitioned to slugging) and/or in the vicinity of walls.[2] Although not the focus of this study, wall effects can be incorporated easily using the methodology discussed through (a) wall-correction factor in Equation 10 based on the size and spatial location of a bubble and (b) revised transfer coefficients for characterizing solids downflow around bubbles in the vicinity of walls.

Note that bubble edges are not well-defined discontinuities and bubble void threshold ε_{gb} in the range 0.7-0.8 is common in literature. In,[38] it is shown that as ε_{gb} is increased from 0.7 to 0.8, overall bubble fraction in the bed decreases but the change in average bubble axial velocity is minimal because sizes of the larger bubbles are relatively unaffected. It follows that correlation coefficient c_1 is weakly dependent on the choice of ε_{gb}. On the other hand, momentum transfer coefficients are computed by spatially averaging (Equation 11) within the region of influence around a bubble, identified using relative time-scale analysis. As ε_{gb} is increased from 0.7 to 0.8, the change in computed c_2 and c_3 is likely to be minimal because the *added* emulsion phase (areas in the vicinity of bubbles with void fraction in the range 0.7-0.8) has relatively low solids fraction and its contribution to c_2 and c_3 will be small.
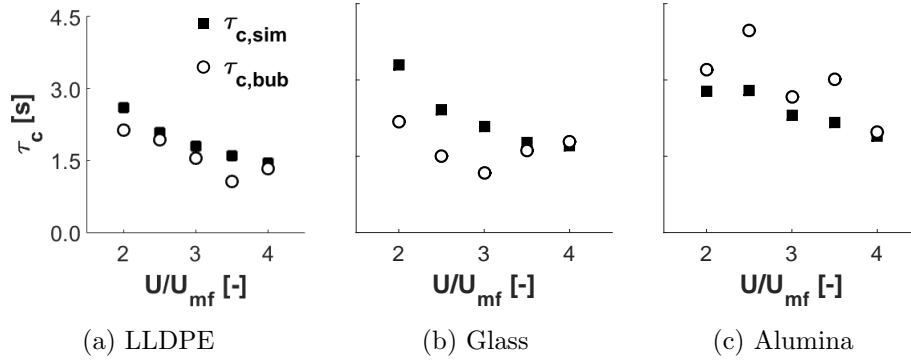
16

Figure 15: Comparison of average circulation time estimated from bubbling dynamics $\tau_{c,bub}$ using Equation 17 with $\tau_{c,sim}$ predictions directly from simulation data using Equation 21.

Applicability

In summary, the mechanistic model developed here correlates solids mixing with bubbling dynamics. Based on the gas (bubble) distribution statistics, the correlation coefficient c_1 and velocity-averaged bubble diameter $\bar{D}_{bv}$ are first computed using Equations 10 and 15, respectively. Subsequently, the average solids axial velocity and circulation time in the bed are computed using Equations 14 and 16 as:

$$\langle v_s^+ \rangle = c_1 c_2 \, 0.71 \sqrt{g \bar{D}_{bv}}$$

$$\tau_{c,bub}^+ = \frac{H_0}{\langle v_s^+ \rangle} = \frac{H_0}{c_1 c_2 \, 0.71 \sqrt{g \bar{D}_{bv}}}$$

where $c_2 \approx [0.4, 0.6]$ (downflow estimates can be obtained similarly). Coefficients characterizing bubbling dynamics c_1 and $\bar{D}_{bv}$ are convenient to measure or estimate using intrusive techniques such as optical and pressure probes or non-intrusive techniques such as capacitance tomography, X-Ray and MRI. Since the numerical simulations presented here show $c_2 \approx 0.4$-0.6 for all three particles (which have disparate Archimedes numbers), it is likely that similar range is applicable to bubbling fluidization of other Geldart B particles. Also note that the mixing model developed implicitly accounts for gas distributor effects (and other operating scenarios) on the reactor-scale solids mixing. This is because changes in gas distribution will result in different bubble size and spatial distributions and, hence, different velocity-averaged bubble diameter $\bar{D}_{bv}$.

Overall, this correlation is extremely useful in large pilot and commercial-scale fluidized beds where direct solids measurements are technically challenging and often economically prohibitive. In a similar way, the developed framework can be extended easily for analyzing mixing dynamics in (a) lab-scale reactors with complex geometries, (b) bubbling fluidization of Geldart A (and other Geldart type) particles and (c) more complex reactive particulate flows (e.g. coal and biomass fluidized bed combustion and gasification systems, polymerization reactors and so on). While executing the former will involve suitable modifications to Equations 10 and 11 (e.g. accounting for retarding effect of walls), task (c) will require additional statistical markers to quantify the effect of relative particle properties and concentrations within mixtures of solid particles.

4. Conclusion

Solids mixing is critical to the performance of fluidized bed reactors. However, fundamental understanding of mixing dynamics continues to be lacking because of difficulties in the simultaneous measurements of gas and solids motion, and technical limitations of diagnostics in large pilot and

commercial reactors. This study is focused on the fundamental investigation of bubble-induced solids micromixing and the development of a predictive mechanistic model for quantifying reactor-scale solids mixing using highly resolved data from fine-grid 3D CFD simulations of a pilot-sized 50 cm diameter fluidized bed.

Mixing dynamics are analyzed in detail for the fluidization of three distinct Geldart B particles (1.15 mm LLDPE, 0.50 mm glass and 0.29 mm alumina) at U/U_{mf}=2-4 by investigating the flow-field in and around bubbles using MS3DATA.[37] Based on the framework developed in,[38] the statistical distribution of gas-flow is first discussed. For the fluidization of all the three particles, gas flow through the dense-phase decreases as U/U_{mf} is raised because of higher bubble activity. For the lighter alumina particles, this decrease is compensated by the substantial increase in visible bubble flow and the observed fast-bubbling regime is consistent with experimental findings in the literature. On the other hand, heavier glass and LLDPE particles show significant increase in gas bypass; throughflow can reach 30-50% of the superficial gas flow with 2-3× shorter residence time as U/U_{mf} increases from 2 to 4. This inhomogeneity in gas mixing results in inefficient gas-solids contacting and consequently, suboptimal solids mixing.

Fundamental investigation of the flow-field around individual bubbles shows that solid particles are driven upwards in the nose and wake regions while downflow is predominantly along the bubble walls. Further, the hydrodynamic characteristics within these micromixing zones are dependent largely on the particle and bubble properties, and are relatively independent of the superficial gas flow. Based on this observation, a mechanistic model is developed which predicts reactor-scale solids circulation by integrating local bubble-induced micromixing contributions over their size and spatial distributions. This model accounts for (a) the influence of global operating conditions though the bubble velocity-diameter correlation and (b) the momentum imparted by each rising bubble onto the surrounding dense-phase through *momentum transfer* coefficients. The latter characterize the hydrodynamics within the region of influence around a bubble, which is identified to be within 30 particle diameters from the bubble boundary based on non-dimensional time-scale (inertial number) analysis. Comparison with circulation time estimates obtained directly from simulation data shows that the developed model (based on bubbling dynamics) is able to capture solids mixing and its dependence on superficial gas-flow in excellent agreement. Overall, by accounting for the bubble size and velocity distributions (through the velocity-averaged bubble diameter), the solids modeling framework implicitly accounts for any changes in gas-flow distribution induced by changes in operating conditions, gas distributor design and/or other geometric factors. Therefore, this correlation between solids mixing and gas (bubble) distribution can be extended easily to analyze axial and lateral mixing in more complex reactive particulate systems and will be particularly useful in large-scale applications where direct solids measurements are often prohibitive.

5. Acknowledgment

6. References

[1] D. Kunii and O. Levenspiel. *Fluidization Engineering.* 1991.

[2] A. Bakshi, C. Altantzis, R.B. Bates, and A.F. Ghoniem. Study of the effect of reactor scale on fluidization hydrodynamics using fine-grid CFD simulations based on the two-fluid model. *Powder Technology*, 299:185 – 198, 2016.

[3] H.R. Norouzi, N. Mostoufi, Z. Mansourpour, R. Sotudeh-Gharebagh, and J. Chaouki. Characterization of solids mixing patterns in bubbling fluidized beds. *Chemical Engineering Research and Design*, 89(6):817 – 826, 2011.

[4] O. Oke, P. Lettieri, P. Salatino, R. Solimene, and L. Mazzei. Numerical simulations of lateral solid mixing in gas-fluidized beds. *Chemical Engineering Science*, 120(0):117 – 129, 2014.

[5] E. Sette. *Solids Mixing in Bubbling Fluidized Beds*. PhD thesis, Chalmers University of Technology, 2016.

[6] M. Liu, Y. Zhang, H. Bi, J. R. Grace, and Y. Zhu. Non-intrusive determination of bubble size in a gassolid fluidized bed: An evaluation. *Chemical Engineering Science*, 65(11):3485 – 3493, 2010.

[7] L. Shen and M. Zhang. Effect of particle size on solids mixing in bubbling fluidized beds. *Powder Technology*, 97(2):170 – 177, 1998.

[8] K. S. Lim, V. S. Gururajan, and P. K. Agarwal. Mixing of homogeneous solids in bubbling fluidized beds: Theoretical modelling and experimental investigation using digital image analysis. *Chemical Engineering Science*, 48(12):2251 – 2265, 1993.

[9] D. Pallares and F. Johnsson. A novel technique for particle tracking in cold 2-dimensional fluidized bedssimulating fuel dispersion. *Chemical Engineering Science*, 61(8):2710 – 2720, 2006.

[10] E. Sette, D. Pallares, and F. Johnsson. Experimental evaluation of lateral mixing of bulk solids in a fluid-dynamically down-scaled bubbling fluidized bed. *Powder Technology*, 263:74 – 80, 2014.

[11] J. Baeyens and D. Geldart. Particle mixing in a gas fluidized bed. *La Fluidisation et ses applications*, pages 182–195, 1974.

[12] J. Werther. Convective solids transport in large diameter gas fluidized beds. *Powder Technology*, 15(2):155 – 167, 1976.

[13] M Stein, Y.L Ding, J.P.K Seville, and D.J Parker. Solids motion in bubbling gas fluidised beds. *Chemical Engineering Science*, 55(22):5291 – 5300, 2000.

[14] A. Soria-Verdugo, L.M. Garcia-Gutierrez, S. Sanchez-Delgado, and U. Ruiz-Rivas. Circulation of an object imersed in a bubbling fluidized bed. *Chemical Engineering Science*, 66(1):78–87, 2011.

[15] Z. Amiri, S. Movahedirad, and M. Shirvani. Particles mixing induced by bubbles in a gas-solid fluidized bed. *AIChE Journal*, 62(5):1430–1438, 2016.

[16] S. Sanchez-Delgado, C. Marugn-Cruz, A. Acosta-Iborra, and D. Santana. Dense-phase velocity fluctuation in a 2-d fluidized bed. *Powder Technology*, 200(12):37 – 45, 2010.

[17] P.N. Rowe, B.A. Partiridge, A.G. Cheney, G.A. Henwood, and E. Lyall. The mechanisms of solid mixing in fluidized beds. *Transactions of the Institute of Chemical Engineers*, 43:271–286, 1965.

[18] L. Shen, M. Zhang, and Y. Xu. Solids mixing in fiuidized beds. *Powder Technology*, 84:207–212, 1995.

[19] L. R. Glicksman and T. Yule. Prediction of the particle flow conditions in the freeboard of a freely bubbling fluidized bed. *Chemical Engineering Science*, 50(1):69 – 79, 1995.

[20] J. C. Abanades, , and G. S. Grasa. Modeling the axial and lateral mixing of solids in fluidized beds. *Industrial & Engineering Chemistry Research*, 40(23):5656–5665, 2001.

[21] D. Santana, S. Nauri, A. Acosta, N. Garca, and A. Macas-Machn. Initial particle velocity spatial distribution from 2-d erupting bubbles in fluidized beds. *Powder Technology*, 150(1):1 – 8, 2005.

[22] J.A. Almendros-Ibez, S. Snchez-Delgado, C. Sobrino, and D. Santana. Experimental observations on the different mechanisms for solid ejection in gas-fluidized beds. *Chemical Engineering and Processing: Process Intensification*, 48(3):734 – 744, 2009.

[23] L.M. Garcia-Gutierrez, A. Soria-Verdugo, N. Garcia-Hernando, and U. Ruiz-Rivas. Simulation of object motion in a bubbling fluidized bed using a monte carlo method. *Chemical Engineering Science*, 96:26 – 32, 2013.

[24] A. Soria-Verdugo, L.M. Garcia-Gutierrez, N. Garca-Hernando, and U. Ruiz-Rivas. Buoyancy effects on objects moving in a bubbling fluidized bed. *Chemical Engineering Science*, 66(12):2833 – 2841, 2011.

[25] I. Julin, J. Herguido, and M. Menndez. Experimental and simulated solids mixing and bubbling behavior in a scaled two-section two-zone fluidized bed reactor. *Chemical Engineering Science*, 143:240 – 255, 2016.

[26] F. Berruti, D. S. Scott, and E. Rhodes. Measuring and modelling lateral solid mixing in a three-dimensional batch gas - solid fluidized bed reactor. *The Canadian Journal of Chemical Engineering*, 64:48–56, 1986.

[27] J. Olsson, D. Pallares, and F. Johnsson. Lateral fuel dispersion in a large-scale bubbling fluidized bed. *Chemical Engineering Science*, 74:148 – 159, 2012.

[28] E. Sette, D. Pallares, and F. Johnsson. Experimental quantification of lateral mixing of fuels in fluid-dynamically down-scaled bubbling fluidized beds. *Applied Energy*, 136:671 – 681, 2014.

[29] R. W. Breault. A review of gassolid dispersion and mass transfer coefficient correlations in circulating fluidized beds. *Powder Technology*, 163(12):9 – 17, 2006.

[30] G Grasa and J C. Abanades. The use of two different models to describe the axial mixing of solids in fluidised beds. *Chemical Engineering Science*, 57(14):2791 – 2798, 2002.

[31] F. Hernndez-Jimnez, S. Snchez-Delgado, A. Gmez-Garca, and A. Acosta-Iborra. Comparison between two-fluid model simulations and particle image analysis & velocimetry (piv) results for a two-dimensional gassolid fluidized bed. *Chemical Engineering Science*, 66(17):3753 – 3772, 2011.

[32] M. Askarishahi, M. Salehi, H. R. Godini, and G. Wozny. CFD study on solids flow pattern and solids mixing characteristics in bubbling fluidized bed: Effect of fluidization velocity and bed aspect ratio. *Powder Technology*, 274:379 – 392, 2015.

[33] J. Sanchez-Prieto, F. Hernandez-Jimenez, L.M. Garcia-Gutierrez, and A. Soria-Verdugo. Experimental study on the characteristic mixing time of solids and its link with the lateral dispersion coefficient in bubbling fluidized beds. *Chemical Engineering Journal*, 307:113 – 121, 2017.

[34] A. Bakshi, C. Altantzis, and A.F. Ghoniem. Towards accurate three-dimensional simulation of dense multi-phase flows using cylindrical coordinates. *Powder Technology*, 264(0):242 – 255, 2014.

[35] C. Altantzis, R.B. Bates, and A.F. Ghoniem. 3D Eulerian modeling of thin rectangular gas-solid fluidized beds: Estimation of the specularity coefficient and its effects on bubbling dynamics and circulation times. *Powder Technology*, 270, Part A(0):256 – 270, 2015.

[36] A. Bakshi, C. Altantzis, R.B. Bates, and A.F. Ghoniem. Eulerian-Eulerian simulation of dense solidgas cylindrical fluidized beds: Impact of wall boundary condition and drag model on fluidization. *Powder Technology*, 277(0):47 – 62, 2015.

[37] A. Bakshi, C. Altantzis, R.B. Bates, and A.F. Ghoniem. Multiphase-flow Statistics using 3D Detection and Tracking Algorithm (MS3DATA): Methodology and application to large-scale fluidized beds. *Chemical Engineering Journal*, 293:355 – 364, 2016.

[38] A. Bakshi, C. Altantzis, L.R. Glicksman, and A.F. Ghoniem. Gas-flow distribution in bubbling fluidized beds: CFD-based analysis and impact of operating conditions. *Powder Technology*, pages –, 2017.

[39] M. Syamlal, W. Rogers, and T. J. O'Brien. *MFIX Documentation Theory Guide*, 1993.

[40] D.G. Schaeffer. Instability in the evolution equations describing incompressible granular flow. *Journal of Differential Equations*, 66:19–50, 1987.

[41] D. Gidaspow. *Multiphase Flow and Fluidization: Continuum and Kinetic Theory Descriptions.* Boston: Academic, 1994.

[42] P.C. Johnson and R. Jackson. Frictional collisional constitutive relations for granular materials, with application to plane shearing. *Journal of Fluid Mechanics*, 176:67–93, 1987.

[43] T. Li and S. Benyahia. Revisiting Johnson and Jackson boundary conditions for granular flows. *AIChE Journal*, 58(7):2058–2068, 2012.

[44] S. Mori and C.Y. Wen. Estimation of the bubble diameter in gaseous fluidized beds. *AIChE Journal*, 21:109–115, 1975.

[45] A.C. Rees, J.F. Davidson, J.S. Dennis, P. S Fennell, L.F. Gladden, A.N. Hayhurst, M.D. Mantle, C.R. Mller, and A.J. Sederman. The nature of the flow just above the perforated plate distributor of a gas-fluidised bed, as imaged using magnetic resonance. *Chemical Engineering Science*, 61(18):6002 – 6015, 2006.

[46] M. Syamlal. *MFIX Documentation Numerical Technique*, January 1998.

[47] J.A. Laverman, X. Fan, A. Ingram, M. van Sint Annaland, D.J. Parker, J.P.K. Seville, and J.A.M. Kuipers. Experimental study on the influence of bed material on the scaling of solids circulation patterns in 3d bubbling gassolid fluidized beds of glass and polyethylene using positron emission particle tracking. *Powder Technology*, 224:297 – 305, 2012.

[48] Martin Rdisli, Tilman J. Schildhauer, Serge M.A. Biollaz, and J. Ruud van Ommen. Bubble characterization in a fluidized bed by means of optical probes. *International Journal of Multiphase Flow*, 41(0):56 – 67, 2012.

[49] J. Baeyens and S.Y. Wu. Bed expansion and the visible bubble flow rate in gas fluidized beds. *Advanced Powder Technology*, 3(3):163 – 189, 1992.

[50] J.A. Almendros-Ibanez, D. Pallares, F. Johnsson, and D. Santana. Voidage distribution around bubbles in a fluidized bed: Influence on throughflow. *Powder Technology*, 197(12):73 – 82, 2010.

[51] P. Jop, Y. Forterre, and O. Pouliquen. A constitutive law for dense granular flows. *Nature*, 441:727–730, 2006.